RSC Advances

PAPER

View Article Online
View Journal | View Issue

Cite this: *RSC Adv.*, 2025, **15**, 3183

Magnesium-ion-doped silica nanosheets as degradable drug carriers with enhanced antibacterial activity and cellular uptake

Ruohan Liao, †[a] Chengdong Zhang,†[a] Zechuang Wang,[a] Xingping Li,[b] Chao Pu,[a] Xuwei Luo,[a] Gang Feng,[a] Qiang Su*[a] and Dongqin Xiao*[a]

Mesoporous silica nanoparticles (MSNs) have attracted significant interest in drug delivery applications due to their good biocompatibility and high specific surface area. However, conventional MSNs typically have small pore sizes and low degradation rates, resulting in limited drug loading capacity and potential *in vivo* nanoparticle accumulation. This study focuses on the synthesis of novel magnesium (Mg) ion-doped silica nanoparticles (MgMSNs) using a chemical precipitation method followed by calcination. In contrast to the nanorod-shaped MSNs, the Mg ion-doped silica nanoparticles exhibited a nanosheet-shaped morphology. When the added Mg^{2+} concentration was 5 mM, the prepared nanosheets (5MgMSNs) showed superior antibacterial activity and increased curcumin-loading capacity compared to pure silica nanoparticles. Additionally, the natural green fluorescence of curcumin allowed for the visualization of cellular uptake, confirming the efficient internalization of 5MgMSNs by L929 cells. Notably, under acidic conditions, the release of Mg ions and the degradability of the nanoparticles were enhanced, indicating pH-responsive release behavior. Overall, these results highlight the favorable degradability and improved cellular uptake capacity of nanosheet Mg-incorporated silica nanoparticles, suggesting their potential for loading polyphenol drugs such as curcumin and achieving efficient drug release within cells.

Received 25th October 2024
Accepted 13th January 2025

DOI: 10.1039/d4ra07626e

rsc.li/rsc-advances

Introduction

Due to the unique advantages of nanomaterials in drug delivery, diagnostics, and targeted therapy, an increasing number of nanomaterials have been developed as drug carriers to overcome the major challenges of traditional medical treatment, such as low drug delivery and undesirable drug biodistribution. Among the various nanocarriers, mesoporous silica nanoparticles (MSNs) have attracted extensive attention due to their excellent biocompatibility, mesoporous structure, high surface area, and modifiable surface chemistry.[1] However, the stable Si–O–Si structure within silica nanoparticles makes them resistant to degradation, leading to potential accumulation in the body and causing acute or subacute inflammation and even toxicity.[2] Additionally, the pore size of traditional mesoporous silica is small (2–6 nm), making it difficult for drug molecules to diffuse into the pores. Also, the drug release from the pores is a simple diffusion process, which cannot realize on-demand release at the lesion sites. Therefore, the development of biodegradable silicate nanoparticles with controlled drug release is great of importance for clinical application. In recent years, researchers have discovered that the incorporation of organic or inorganic moieties into silica nanoparticles can reconstruct the silica framework and improve its degradability.[3] For instance, Park *et al.* successfully synthesized polyurethane-silica hybrids with good mechanical properties that are completely biodegradable for bone regeneration.[4] Rahmani *et al.* successfully synthesized degradable organosilica nanoparticles by the co-condensation of bis-(triethoxysilyl) ethane and the bis(3-(triethoxysilyl) propyl) tetrasulfide.[5] However, the synthesis process is rather intricate, involving multiple steps that could potentially impact the reproducibility and cost-effectiveness of production. Additionally, organic silane precursors such as bis-(triethoxysilyl) ethane exhibit a certain level of toxicity, may pose health hazards during handling and utilization, potentially endangering human well-being. In recent years, some efforts have been made to improve the degrability of MSNs *via* change the composition *via* doping metallic ions. Yu *et al.* found that Mn-doped MSNs rapidly disintegrated in the tumor microenvironment, making them suitable for cancer diagnosis and treatment.[6] However, high Mn ions release from the nanoparticles may result in potential cytotoxicity to normal cells[7]. Thus, ideal metallic ions for engineering silica frameworks should possess high biocompatibility and be abundant in the human body, such as Na, Fe, and Mg. As the essential elements in human metabolism, Mg deficiency can lead to excessive bone

[a]*Research Institute of Tissue Engineering and Stem Cells, Department of Pharmacy, The Second Clinical College of North Sichuan Medical College, Nanchong, Sichuan 637000, China. E-mail: xiaodongqin@nsmc.edu.cn; 187169442@qq.com*
[b]*Department of Orthopaedics, Chengfei Hospital, Chengdu, Sichuan 610091, China*
† Authors contributed equally to this work.

resorption and osteoporosis.[8] Magnesium promotes osteogenic differentiation mediated by calcitonin gene-related peptide (CGRP),[9] inhibits osteoclast activity,[10] facilitates fibroblast migration,[11] and promotes angiogenesis.[12] Furthermore, magnesium exhibits antibacterial properties by preventing bacterial adhesion and inhibiting biofilm formation.[13,14] Therefore, Mg is a promising candidate for engineering silica frameworks to obtain biofunctional nanoparticles for safer medical treatment. Also, the Mg–O bond is easily broken under mild acidic environment, which benefits for altering the physicochemical property and enhancing the biodegradability of MSNs.

Studies also have demonstrated a close correlation between the morphology of nanoparticles and their physicochemical property and biofunctions.[15] For instance, macrophages exhibit lower uptake efficiency for worm-shaped nanoparticles compared with spherical nanoparticles in the report of Champion *et al.*[16] Adnan *et al.* discovered that rod-shaped and star-shaped gold nanoparticles showed superior photothermal therapy and drug delivery efficacy compared with spherical gold nanoparticles.[17] Zhang *et al.* found that needle-like PLGA-PEG nanoparticles achieved significantly greater cytotoxicity than spherical nanoparticles by disrupting lysosomes.[18] Also, dendritic mesoporous silica nanoparticles exhibited enhanced degradability in comparison of spherical nanoparticles.[19] Therefore, preparation of silica-based nanoparticles with new morphologies is crucial to develop new functions.

Herein, a simple method was reported to synthesize biodegradable nanosheet-shaped silica-based nanoparticles by *in situ* Mg-ions-doping. The introduction of Mg ions not only changed the morphology, but also improved the degradability and antibacterial activity of the nanoparticles. Also, curcumin as a model of polyphneol drugs was loaded in the MgMSNs. Compared with MSNs, the MgMSNs showed an increasing drug-loading capacity and enhanced cellular uptake, indicating high therapeutic efficiency. Therefore, these Mg-doped silica nanosheets have promising potential application in polyphenol drugs delivery and tissue regeneration.

Materials and methods

Materials

Hexadecyl trimethyl ammonium Bromide (CTAB), tetraethyl orthosilicate (TEOS), and ethanol were obtained from Sigma Corporation. Magnesium nitrate hexahydrate ($Mg(NO_3)_2 \cdot 6H_2O$), ammonia solution (28 wt%), and ethanol were obtained from Sichuan Kelun Pharmaceutical Co. Curcumin (Adamas-beta, China) were purchased from Discovery Platform.

Preparation of MgMSNs

First, CTAB was dissolved in 75 mL of deionized water and heated to 90 °C until clear. After stirring for 30 min, 3 mL of ammonia solution (28 wt%) was added to the solution, followed by stirring for another 30 min. Then, $Mg(NO_3)_2 \cdot 6H_2O$ (5 mM, 10 mM and 15 mM) were added to the solution and stirred for 30 min. Subsequently, 1.2 mL of TEOS was added to the solution, and stirred for 24 h. The resulting particles were collected after centrifugation and washed three times with ethanol and deionized water, respectively. After vacuum freeze-drying, the particles were calcined at 650 °C for 3 h with a heating rate of 2 °C min^{-1}. The obtained sample was named as 5MgMSNs, 10MgMSNs and 15MgMSNs, respectively. The same procedure without the addition of $Mg(NO_3)_2 \cdot 6H_2O$ was used to obtain SiO_2 (MSNs).

Characterization of MgMSNs

To observe the morphology of the nanoparticles, the samples were dispersed in anhydrous ethanol and dropped onto a silicon wafer. After thoroughly drying, the silicon wafer was sputter-coated with gold, and then observed using a scanning electron microscope (SEM, Thermo Scientific, Apreo 2S). The elemental analysis of the samples was determined with an energy dispersive spectroscopy (EDS) attached to the SEM. Also, the nanoparticles were dispersed in anhydrous ethanol, dropped onto a copper grid, and observed under a transmission electron microscopy (TEM, FEI-Tecnai G2 F20). To determine the product phase, the samples were ground and pressed into pellets, and measured using X-ray diffraction (XRD Rigaku Ultima IV, CuKα, 40 kV, 40 mA) with 2θ angle range of 5–90. The chemical composition of the sample was determined by Fourier-transform infrared spectrometer (FT-IR, MFT-2000, JASCO Co., Japan, 4000–400 cm^{-1}) using KBr pellets. Also, the elemental composition of the samples was determined using X-ray photoelectron spectroscopy (XPS, EscaLab 250Xi, Thermo Scientific K-Alpha, America, 0–1200 eV). The surface area and pore size distribution of the samples were measured using nitrogen adsorption and desorption (Micromeritics ASAP 2460). The particle size was determined by dynamic light scattering (DLS, Malvern Panalytica, Zetasizer Zs90, Britain).

In vitro degradation of MgMSNs

In order to investigate the effect of pH on the degradation behavior of MSNs, the nanoparticles were immersed in physiological saline solutions with different pH values (pH 7, 5). The samples were placed in a vibrating incubator at 37 °C. At specified time intervals, 3 mL of the solution was taken from each sample for observation. The morphology variation of the nanoparticles was observed using SEM, while the ions released from the nanoparticles were measured using atomic absorption Spectroscopy (AAS, AA-7000, Shimadzu, Japan).

Drug loading efficiency and the encapsulation efficiency

Under dark conditions, 10 mg of MgMSNs was dispersed in 10 mL of curcumin solution dissolved in ethanol (0.5 mg mL^{-1}). After 24 h of stirring, the curcumin-loaded MgMSNs were collected by centrifugation, and the supernatant was collected for evaluating curcumin loading efficiency. The curcumin concentration in the supernatant was measured using a UV-visible spectrophotometer (UV2700i, Hitachi, Japan) at a wavelength of 470 nm.

Cell culture

L929 cells were cultured in Dulbecco's modified Eagle medium (DMEM, Gibco Company, America) supplemented with 10% fetal bovine serum (FBS, Shanghai Viva Cell Biosciences Ltd) and 1% penicillin-streptomycin (PS, Shanghai VivaCell Biosciences Ltd). The cells were incubated at 37 °C with 5% CO_2 in a humidified incubator. In all experiments, 0.25% trypsin (Gibco Company) was used to collect the cells, which were then resuspended in fresh culture medium for subsequent culturing and experiments.

Cytotoxicity evaluation of MgMSNs

L929 cells were seeded in a 96-well plate at a density of 5000 cells per well and incubated in DMEM culture medium containing 10% FBS for 24 h. Then, 100 μL of nanoparticle-containing culture medium (concentration 100 μg mL^{-1}) was added to each well. After 24 h of incubation, the CCK-8 assay kit (Vazyme, China) was utilized for assessing cellular proliferation in accordance with the operation instructions. The absorbance of the supernatant at 450 nm was measured using a microplate reader (Allsheng Feyond-A300, China) to determine cell viability.

In vitro cellular uptake of MgMSNs

L929 cells were seeded in a 24-well plate at a density of 1×10^5 cells per well. After 24 h, the culture medium was removed, and 1 mL of fresh medium containing SiO2@CUR or 5MgMSNs@CUR (100 μg mL^{-1}) was added. After 12 h of incubation, the culture medium was removed, and the cells were washed three times with PBS. DAPI staining was performed for 15 min to label the cell nuclei. Finally, the cells were washed three times with PBS and observed using confocal microscopy (Olympus FV3000, Japan).

Antibacterial effect of MgMSNs

After resuspending SiO_2 and 5MgMSNs in fresh Luria-Bertani broth (Shanghai Aladdin Biochemical Technology Co), 1 mL of the suspension was taken and sonicated, followed by transfer into a 48-well plate. Subsequently, 50 μL of *S. aureus* (ATCC 25923) or *E. coli* (ATCC 25922) broth was added to each well, and the plate was incubated on a shaking incubator at 37 °C for 5 h. After incubation, 50 μL of the bacterial suspension was spread onto agar plates for colony counting. Meanwhile, 200 μL of the bacterial suspension was taken and subjected to live/dead staining (Maokangbio MX4234), followed by observation under a fluorescence microscope.

To observe the morphology of the bacteria, bacterial suspension was transferred onto silicon wafers, fixed in 4% paraformaldehyde at 4 °C for 4 h, followed by dehydrating in sequential baths of 50%, 70%, 90%, and 100% ethanol for 30 min each. Subsequently, the samples were sputter coated using gold and observed using SEM.

After co-culturing the nanoparticles dispersed in PBS with bacteria (5×10^9 cells, concentrated 5 mL culture) at 37 °C for 60 min, flow cytometry was used for detection. Then, 100 μL of the treated culture were added into 900 μL of normal saline and analyzed using flow cytometry (ACEA NovoCyte 3L13C). For the dot plot, the *X*-axis reflects the logarithmic scale of FSC (forward scatter) intensity, and the *Y*-axis corresponded to the linear scale of SSC (side scatter) intensity. The gating of the data as P1 and P2 was based on SSC and FSC from the control group, allowing us to distinguish cells that had internalized nanoparticles (P1) from those that were not internalized or had adsorption (P2).[20] No compensation was performed during the experiment.

Results and discussion

Synthesis and characterization of MgMSNs

During the synthesis process of mesoporous silica, CTAB is commonly used as a structure-directing and pore-forming agent, while TEOS serves as the precursor for SiO_2. In this study, different concentrations of Mg ions were added into the solution during the preparation of mesoporous silica, resulting in the fabrication of MgMSNs using a one-pot method. It has been reported that the Mg–O bond is sensitive to weakly acidic environments and can be broken under acidic conditions.[21] Previous studies have indicated that both the skin and tumor microenvironments are weakly acidic.[22,23] Therefore, in a weakly acidic environment, Mg^{2+} are easily released from the framework of MgMSNs, leading to rapid particle structure collapse and accelerated breakage of the –Si–O–Si– bonds in MgMSNs, thereby promoting the drugs release round the chronic wound or tumor area.

SEM images demonstrated that MgMSNs exhibit a sheet-like structure, in contrast to the nanorod shape of SiO_2 nanoparticles (Fig. 1). EDS mapping showed that Mg, O, and Si were uniformly distributed on the MgMSNs (Fig. 1B–D). Moreover, the morphology of MgMSNs remained largely unchanged, with a slight increase in particle size as the concentration of Mg ions increases.

As shown in the EDS analysis (Fig. 2A), the incorporation of Mg into MSNs was approximately 5 wt% for 5MgMSNs. The chemical composition of 5MgMSNs were further investigated

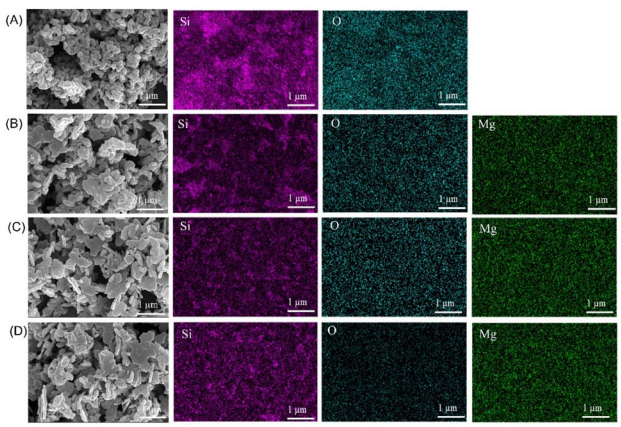

Fig. 1 SEM image and EDS element mapping of SiO_2 nanoparticles (A), 5MgMSNs (B), 10MgMSNs (C), 15MgMSNs (D).

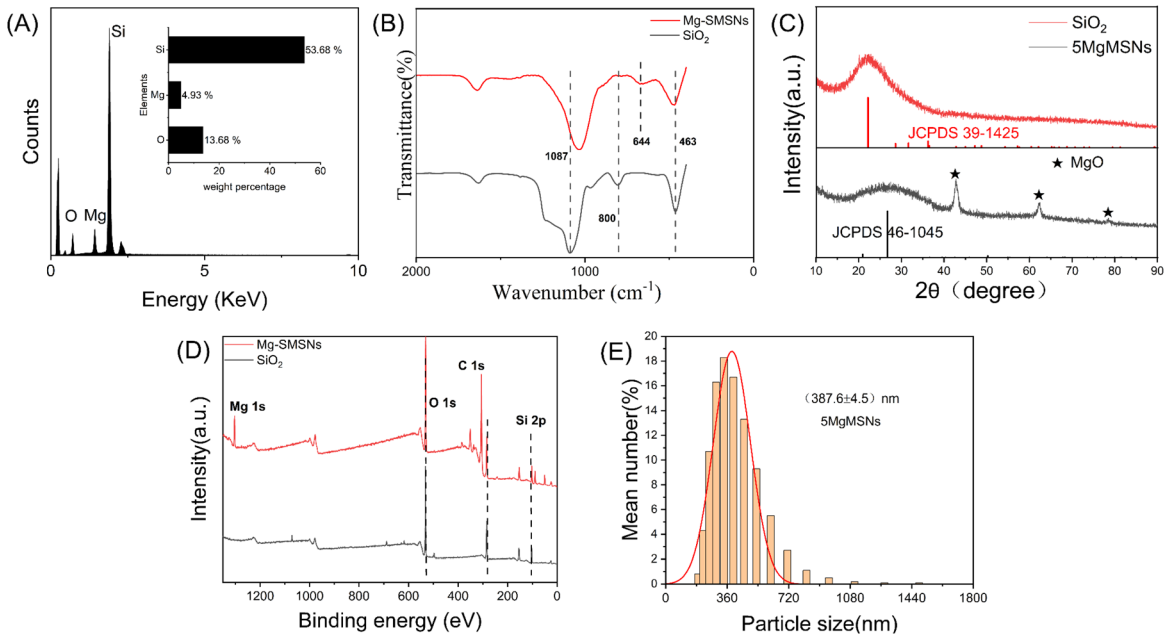

Fig. 2 (A) EDS spectrum of 5MgMSNs, (B) FT-IR spectra of SiO_2 and 5MgMSNs, (C) XRD pattern of SiO_2 and 5MgMSNs, (D) XPS spectrum of SiO_2 and 5MgMSNs, (E) size distribution of the 5MgMSNs.

using XPS. The XPS analysis of Mg-SMSNs (Fig. 2D) revealed the characteristic peaks corresponding to Mg, O, and Si, indicating the successful incorporation of Mg into SiO_2. The XRD spectra (Fig. 2C) showed that broad diffraction peak around 22° was corresponded to SiO_2 (JCPDS 39-1425). However, the broad diffraction peak appeared around 26.6° in the sample of 5MgMSNs, indicating that the Mg addition induced the diffraction peak of SiO_2 to red shift. Also, the sharp diffraction peak at 42.9°, 62.3° and 78.6°matched with MgO (JCPDS 45-0946),confirming the successful incorporation of Mg into MgMSNs sample.[24] A similar phenomenon has also been observed by Yu and his team in manganese-doped silica.[6] FT-IR analysis (Fig. 2B) showed that the absorption band at 800 cm^{-1} and 463 cm^{-1} was related to the Si–O–Si vibrations in amorphous silica, while the strong absorption band at 1087 cm^{-1} corresponds to the symmetric stretching vibration of Si–O.[24,25] In the case of Mg-doped nanoparticles, a broader Si–O–Si band around 1100 cm^{-1} could be observed, which is attributed to increased disorder and reduced aggregation within the silica network due to the introduction of Mg^{2+}.[26] Compared to the FT-IR spectrum of SiO_2, the appearance of an absorption band at 644 cm^{-1} in the FT-IR spectrum of 5MgMSNs was at-tributed to the in-plane bending vibration of Mg–O, indicating the successful preparation of Mg-incorporated MSNs.[24] DLS test results indicated that the particle size of MgMSNs was 387.6 ± 4.5 nm, consistent with the SEM findings (Fig. 2E). TEM image (Fig. 3A) further revealed the characteristics of the 5MgMSNs. The nanosheets exhibited a plate-like structure with a thickness of approximately 10 nm and a particle size of around 300 nm, which is consistent with the results obtained from DLS measurements. The TEM image provided a clear visualization of the mesoporous structure of the 5MgMSNs.

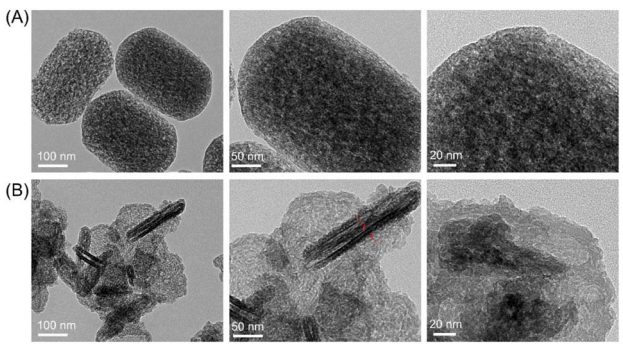

Fig. 3 (A) TEM image of SiO_2 nanoparticles, (B) TEM image of 5MgMSNs. The red arrows indicate the thickness of 5MgMSNs.

Drug loading efficiency and the encapsulation efficiency

The specific surface area and pore size distribution of SiO_2 and 5MgMSNs were analyzed through nitrogen adsorption–desorption experiments, as shown in Fig. 4. Both SiO_2 and 5MgMSNs exhibited type IV isotherms, with a significant hysteresis loop in the P/P0 range of 0.3–0.8, indicating the presence of mesoporous structures in both materials. The specific surface area, mesopore volume, and average pore size of SiO_2 were determined to be 310.94 m^2 g^{-1}, 0.27 cm^3 g^{-1}, and 4.59 nm, respectively. For 5MgMSNs, the specific surface area, mesopore volume, and average pore size were measured to be 316.55 m^2 g^{-1}, 0.41 cm^3 g^{-1}, and 5.54 nm, respectively. The results indicated that the pore size of 5MgMSNs was larger than that of SiO_2 nanoparticles, providing favorable conditions for the loading of large molecular drugs and subsequent degradation processes.

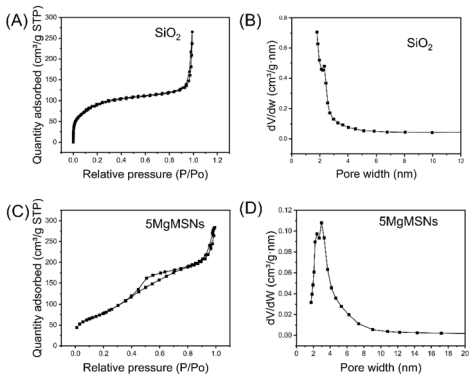

Fig. 4 (A) N_2 adsorption–desorption isotherm and (B) corresponding pore-size distribution of SiO_2. (C) N_2 adsorption–desorption isotherm and (D) corresponding pore-size distribution of 5MgMSNs.

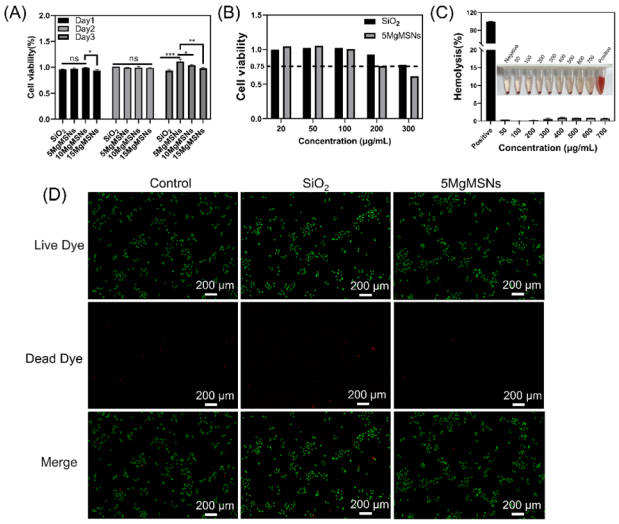

Fig. 5 (A) Cell viabilities of L929 cells after the coincubation with different concentrations of SiO_2 and 5MgMSNs. (B) Cell viabilities of L929 cells after the coincubation with 5MgMSNs, 10MgMSNs and 15MgMSNs. (C) Percentage of hemolysis of erythrocytes after incubation with different concentrations of 5MgMSNs. (D) Representative fluorescent images of HUVEC live/dead cell staining following incubation with 5MgMSNs and SiO_2 (* indicates $p < 0.05$, ** indicates $p < 0.01$, *** indicates $p < 0.001$).

Using curcumin as a model drug, the absorbance of the supernatant before and after drug loading was measured using a UV-visible spectrophotometer. The encapsulation efficiency of 5MgMSNs was calculated to be 67.4%, while the encapsulation efficiency of SiO_2 was 63.3%. These results indicated that, similar to SiO_2, 5MgMSNs exhibited good drug loading efficiency.

Biocompatibility and cytotoxicity of MgMSNs

The toxicity of biodegradation products is of great significance for the biocompatibility of biodegradable 5MgMSNs. The cell viability of 5MgMSNs was assessed through a CCK-8 assay. It was found that even after co-incubation with a high concentration (200 μg mL^{-1}) of 5MgMSNs, the cell viability of L929 cells remained above 75%, indicating the low toxicity of the 5MgMSNs nanocarrier (Fig. 5A). The cell toxicity of MgMSNs doped with different Mg ions concentrations was investigated through the CCK-8 assay, and the results showed that the increase in Mg ions concentrations in MgMSNs had little effect on cell viability (Fig. 5B). Hemolysis assay results demonstrated that even at high concentrations (Fig. 5C), the hemolysis rate of 5MgMSNs remained below 5%, further confirming the excellent blood biocompatibility of 5MgMSNs. The live/dead staining assay was conducted to visualize the viability and morphology of the cells after exposure to 5MgMSNs. The staining results (Fig. 5D) revealed a predominance of green fluorescence, indicating the presence of viable cells with intact plasma membranes. Minimal red fluorescence was observed, indicating dead cells with compromised membrane integrity. The above results further confirm the non-toxicity of 5MgMSNs to various cells and their compatibility with the cell environment.

In vitro degradation of MgMSNs

It has been demonstrated that the Mg–O bond is sensitive to weakly acidic environments. Therefore, the cleavage of Mg–O bonds may generate a large number of defects in the framework of 5MgMSNs, which further serve as degradation sites with an enhanced biodegradation rate, thereby improving the biodegradability of SiO_2.[2] To evaluate the biodegradation behavior of 5MgMSNs, the particles were immersed in PBS at different pH values (pH 7 and 5), and their structural changes were directly observed through SEM. It was found that after incubation in PBS at pH 7 and 5 for 14 days, only small debris of biodegradation products remained for 5MgMSNs, while the structure of SiO_2 showed no significant changes (Fig. 6A). Furthermore, the biodegradation of 5MgMSNs was higher in pH 5 PBS than in pH 7 PBS (Fig. 6A). By monitoring the quantitative biodegradation process using AAS, the results indicated that after 15 days, the Mg ions concentrations were 86.67 μg mL^{-1} at pH 5 and 72.25 μg mL^{-1} at pH 7. Notably, the release of Mg^{2+} from 5MgMSN exhibited pH dependence, with acidic conditions accelerating

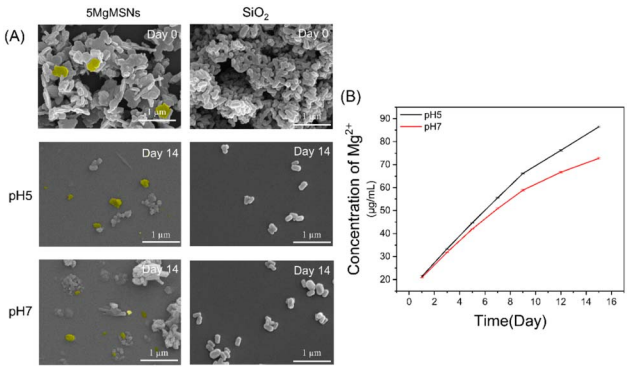

Fig. 6 (A) Biodegradation behavior of 5MgMSNs and SiO_2. Highlighted in yellow are select nanosheets, indicating their transformation pre- and post-degradation. (B) Accumulated releasing profiles of Mg ions.

Mg ions release (Fig. 6B). This result is consistent with the observations from SEM. This characteristic of 5MgMSNs provides possibilities for their rapid degradation in the low pH microenvironment. The pH-responsive degradation behavior of the 5MgMSNs enables selective drug release in the acidic-microenvironment, further enhancing their therapeutic effect.

In vitro cellular uptake of MgMSNs

Metal ions can coordinate with polyphenols to form Metal-Polyphenol Networks (MPNs). MPNs, combining the chemical catalysis and antimicrobial properties of metal ions with the anti-inflammatory and antioxidant properties of polyphenolic compounds, have garnered significant attention in the biomedical fields of anti-tumor, antimicrobial, and anti-inflammatory research.[27,28] Curcumin, as a classic polyphenolic substance, possesses a unique β-diketone structure, enabling it to form a six-membered ring with metal ions through bidentate chelation.[29] The Mg ions in 5MgMSNs can form stable chelates with curcumin, thereby enhancing the bioavailability of curcumin. In synergy with curcumin, they are expected to enhance its antibacterial, anti-inflammatory, and anti-cancer effects.

The formation of a 5MgMSNs-curcumin complex could potentially be employed to develop a drug-controlled release system. This could facilitate the sustained release of curcumin in the body, providing long-term therapeutic effects. Therefore, curcumin was selected as a model drug for *in vitro* cellular uptake studies of 5MgMSNs.

The enhanced cellular uptake of nanoparticles is a crucial advantage for their application as drug carriers. Utilizing the inherent green fluorescence of curcumin, the cellular uptake of SiO_2 and 5MgMSNs nanoparticles by L929 cells was observed. As shown in the figure (Fig. 7A), after 12 of incubation, green fluorescence appeared in the cells treated with 5MgMSNs, indicating that the nanoparticles were internalized by the cells through endocytosis, while in the SiO_2 group, hardly any overlapping green fluorescence with the blue cell nucleus was observed. The results from high-magnification further demonstrated that after cellular uptake of 5MgMSNs@CUR, curcumin was released and entered the cell nucleus (Fig. 7B). This may be attributed to the unique sheet-like structure of 5MgMSNs@CUR. This could be attributed to the unique flake-like structure of 5MgMSNs@CUR, in which the edge length is significantly smaller than the diagonal, thus reducing the time required to overcome the kinetic barrier on the lipid membrane.[30] Some studies have demonstrated that silica nanomaterials with different aspect ratios (ARs) exhibit shape-dependent cellular uptake behavior. Nanoparticles with larger ARs can display faster internalization and higher cellular uptake efficiency, which could explain the aforementioned results.

Antibacterial effect of MgMSNs

The antibacterial properties of nanoparticles against *E. coli* and *S. aureus* were evaluated using the classic agar plate counting method. As shown in the figure (Fig. 8A and 9A), SiO_2 exhibited non-antibacterial activity, while 5MgMSNs demonstrated antibacterial effects. At a concentration of 1 mg mL^{-1}, 5MgMSNs demonstrated an antibacterial efficacy of ~45.7% against *S. aureus* and ~84.1% against *E. coli* (Fig. 8C and 9C). When the concentration was increased to 2 mg mL^{-1}, the antibacterial efficacy against *S. aureus* improved to 95.6%, while the efficacy against *E. coli* reached 96%. Further increasing the concentration to 3 mg mL^{-1} resulted in an antibacterial rate of 99.1% against *S. aureus* and 99.3% against *E. coli*. These results

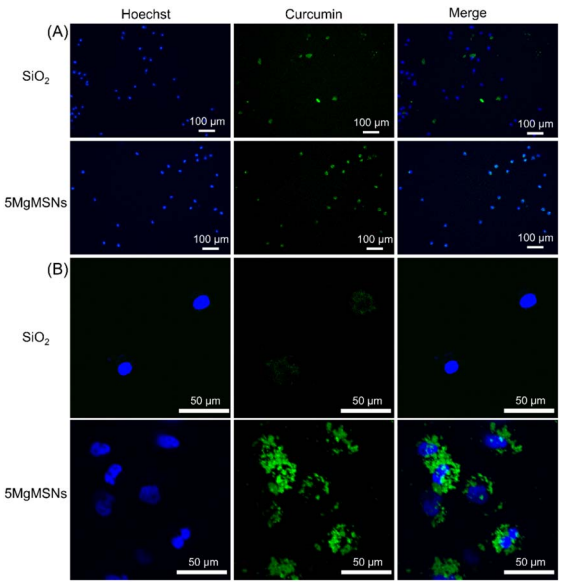

Fig. 7 (A) Representative fluorescent images of L929 cells after coincubation with 5MgMSNs@CUR and SiO_2@CUR for 12 h. (B) CLSM images of L929 cells after coincubation with 5MgMSNs@CUR and SiO_2@CUR for 12 h.

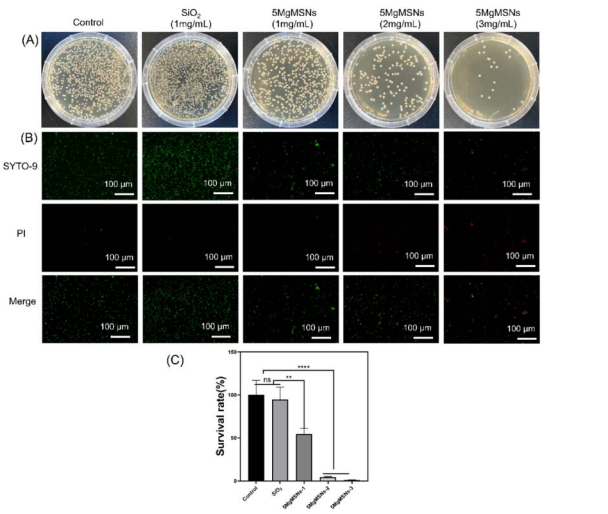

Fig. 8 (A) Representative photographic images of *S. aureus* treated using different nanoparticle. (B) Live–dead staining images of *S. aureus* after different treatments. (C) Viability of *S. aureus* (ns indicates $p > 0.05$, ** indicates $p < 0.01$, **** indicates $p < 0.0001$).

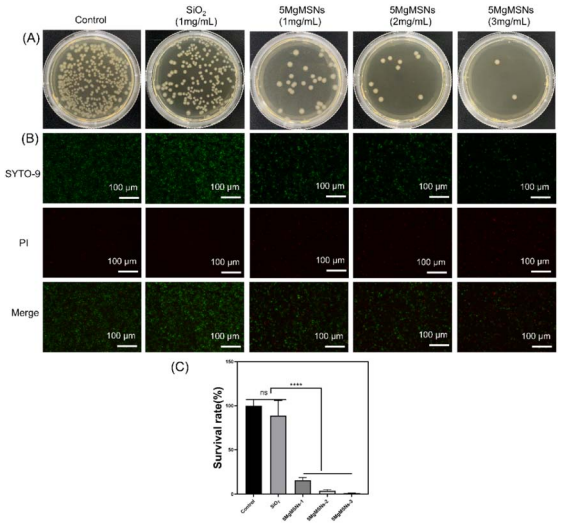

Fig. 9 (A) Representative photographic images of *E. coli* treated using different nanoparticle. (B) Live-dead staining images of *E. coli* after different treatments. (C) Viability of *E. coli* (ns indicates $p > 0.05$, **** indicates $p < 0.0001$).

suggested that the nanosheets exhibited a dose-dependent reduction in bacterial count, indicating their potential as effective antibacterial agents. Live/dead staining additionally confirmed that after treatment with 5MgMSNs, the majority of bacteria were killed (Fig. 8B and 9B), while most bacteria in the other groups remained viable. Based on the above results, it was concluded that 5MgMSNs exhibited obvious antibacterial properties against *S. aureus* and *E. coli.*

Subsequently, the morphology of bacteria was observed using SEM. As depicted in the Fig. 10, post-treatment, the cell wall of *S. aureus* exhibited wrinkles and ruptures, while the cell wall of *E. coli* appeared blurred and collapsed. These observations suggested that 5MgMSNs exhibited antibacterial effects on both Gram-negative and Gram-positive bacteria. Further observations from the SEM images revealed an increased number of nanoparticles surrounding the bacteria in the 5MgMSNs group compared with that in SiO_2 group, indicating a stronger adhesion effect of 5MgMSNs. The nanoparticles adsorption around bacteria could result in cell wall depolarization, enhanced local toxicity, and an alteration in the typical negative charge of the cell wall, thereby increasing its permeability to kill bacteria.[31,32]

To further study the interaction mechanism between the material and bacteria, we employed flow cytometry to detect the uptake of nanoparticles in live bacteria. The relationship between FSC intensity and cell size, as well as SSC intensity and cell granularity and clustering, has been well established.[33] Kumar *et al.* have demonstrated that the intensity of SSC intensity can be utilized as a parameter for detecting nanoparticle internalization in bacteria, while the intensity of FSC intensity can be employed to detect bacterial adherence to nanoparticles.[20] This experimental data (Fig. 11) indicated that after 60 min of nanoparticle treatment, both *S. aureus* and *E. coli* in the SiO_2 group and the 5MgMSNs group exhibited an increase in SSC intensity (indicating granularity) and FSC intensity (indicating adhesion). However, the 5MgMSNs group displayed significantly higher levels compared to the SiO_2 group. The results suggested that once 5MgMSNs were internalized by the bacteria, they might degrade within the bacterial cells, continuously releasing Mg^{2+}, thereby generating considerable osmotic pressure and instigating osmotic lysis to eliminate the bacteria.[32] Based on the findings, it could be deduced that the antibacterial activity of 5MgMSNs is attributable not only to the inherent antimicrobial properties of Mg^{2+} but also potentially to the unique structure of the nanosheets.[13,14,34] The shape and size of nanoparticles have been identified as key factors influencing their interaction with bacteria.[35–37] The

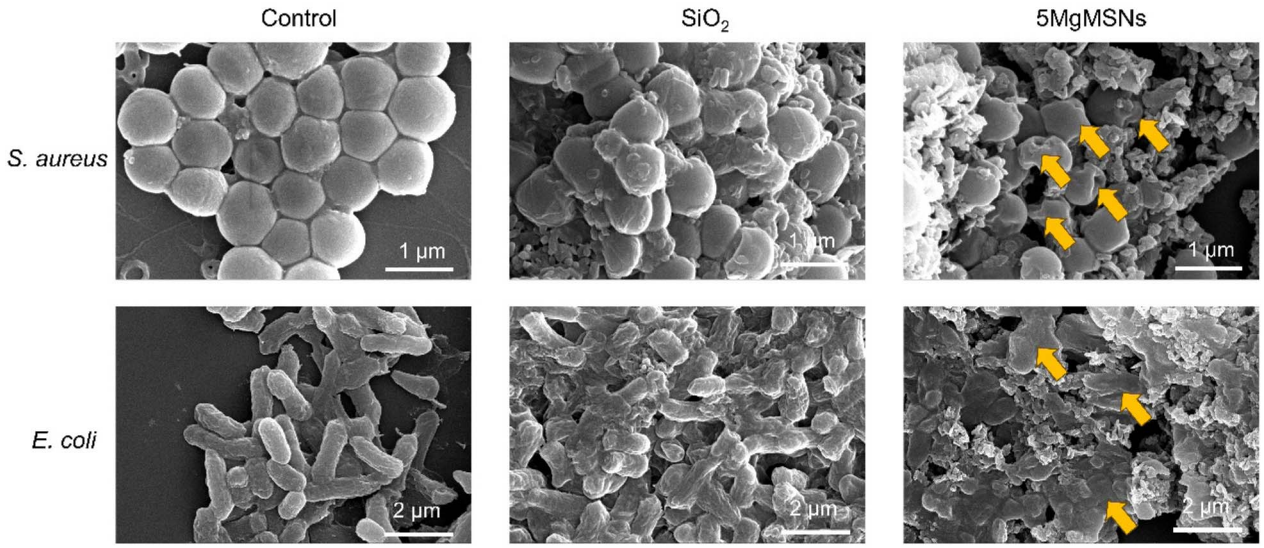

Fig. 10 The SEM images of *S. aureus* and *E. coli* after treatment with nanoparticles (the yellow arrows indicate deformed bacteria).

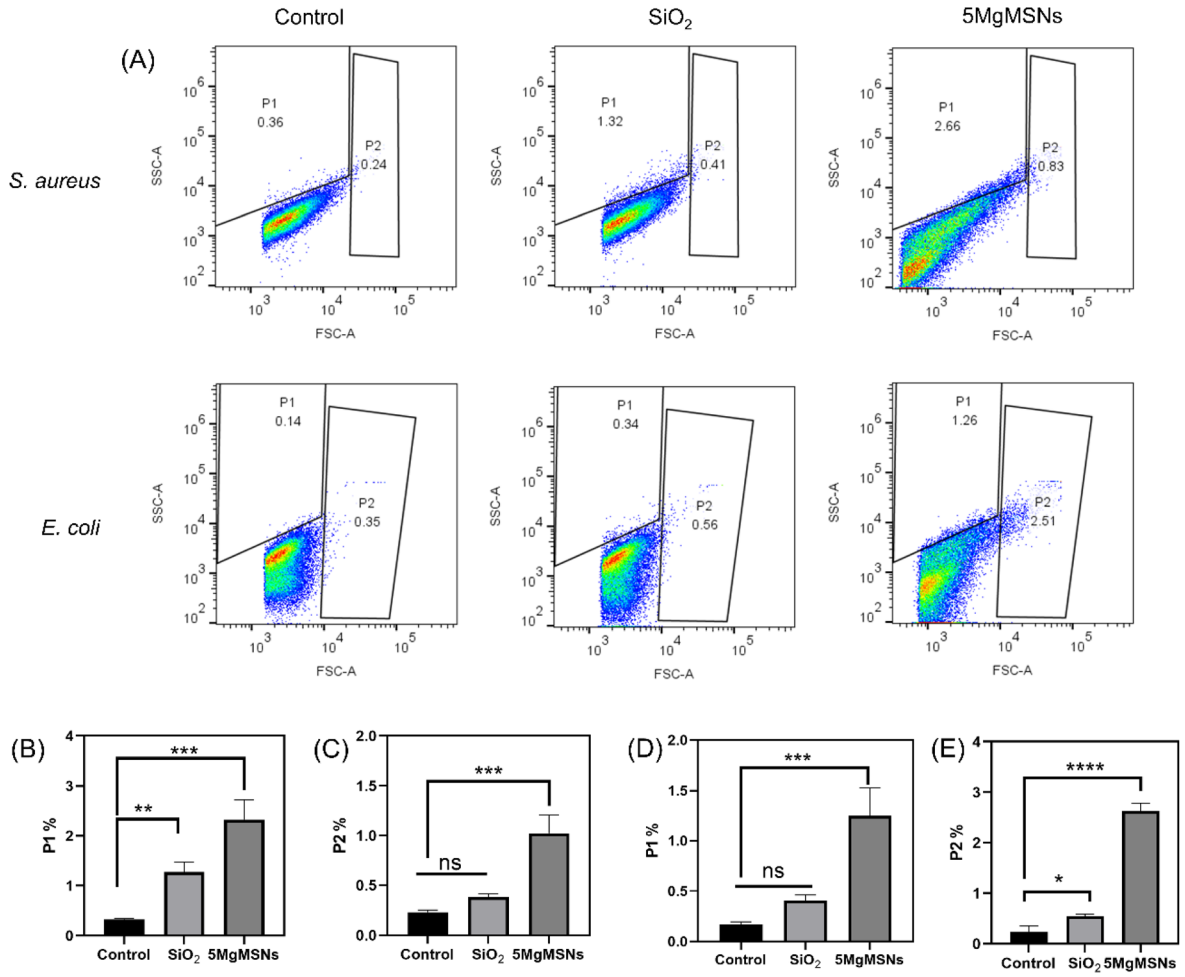

Fig. 11 (A) Scatter analysis of 5MgMSNs and SiO_2 uptake in *S. aureus* and *E. coli* after 60 min. (B and C) Quantitative analysis of P1 (uptake) and P2 (adhesion) of *S. aureus*. (D and E) Quantitative analysis of P1 (uptake) and P2 (adhesion) of *E. coli*.

increased uptake and adhesion capacity of 5MgMSNs also may be the reasons for their antibacterial performance.

Conclusion

In summary, Mg-ion-doped silica nanosheets were successfully prepared using a simple chemical precipitation method. The induction of Mg ions not only significantly improved the degradability of SiO_2 nanoparticles, but also enhanced their antibacterial activity, and cellular uptake ability. Also, these Mg ions-doped SiO_2 nanoparticles showed high affinity with polyphenols. Therefore, these nanosheet-shaped nanoparticles hold great promising application as drug carriers for treatment of various diseases, such as inflammatory diseases and cancer. Further study needs to be carried out to explore the physicochemical and biological properties of these nanosheet-shaped nanoparticles, and to assess their *in vivo* performance for evaluating their therapeutic effects.

Data availability

Data supporting this study are openly available from the corresponding authors.

Author contributions

Ruohan Liao: conceptualization, methodology, investigation, writing–original draft. Chengdong Zhang: conceptualization, methodology, investigation, writing–original draft. Zechuang Wang: methodology, investigation. Xingping Li: methodology, investigation. Chao Pu: validation, investigation. Xuwei Luo: conceptualization, supervision. Qiang Su: conceptualization, methodology, investigation, writing – review & editing. Gang Feng: conceptualization, supervision. Dongqin Xiao: conceptualization, methodology, writing – review & editing and funding acquisition.

Conflicts of interest

The authors declare that they have no known competing financial interests or personal relationships that could have appeared to influence the work reported in this paper.

Acknowledgements

This study was funded by Chunhui Project of the Ministry of Education (HZKY20220558), National Natural Science Foundation of Sichuan Province (2023NSFSC1740), the Medical

Research Project Plan of Sichuan Province (S20012, Q22034), the College-City Cooperation Project of Nanchong City (22SXJCQN0002), Research Fund Project of Genertec Medical (TYYLKYJJ-2022-051), Science and Technology Project of Nanchong City (23JCYJPT0021).

References

1 B. R. Gomes, J. L. Lopes, L. Coelho, M. Ligonzo, M. Rigoletto, G. Magnacca and F. Deganello, *Nanomaterials*, 2023, **13**, 2276.
2 L. Yu, Y. Chen, H. Lin, S. Gao, H. Chen and J. Shi, *Small*, 2018, **14**, 1800708.
3 J. Zhang, K. Tang, Z. Liu, Z. Zhang, S. Duan, H. Wang, H. Yang, D. Yang and W. Fan, *Nanoscale Horiz.*, 2024, **9**, 186–214.
4 S. J. Park, S. H. Im, D. Kim, D. Park, Y. Jung, H. Han, S. H. Kim and J. J. Chung, *NPG Asia Mater.*, 2023, **15**, 28.
5 S. Rahmani, A. Chaix, D. Aggad, P. Hoang, B. Moosa, M. Garcia, M. Gary-Bobo, C. Charnay, A. AlMalik, J.-O. Durand and N. M. Khashab, *Mol. Syst. Des. Eng.*, 2017, **2**, 380–383.
6 L. Yu, Y. Chen, M. Wu, X. Cai, H. Yao, L. Zhang, H. Chen and J. Shi, *J. Am. Chem. Soc.*, 2016, **138**, 9881–9894.
7 W. Chen, W. Xie, Z. Gao, C. Lin, M. Tan, Y. Zhang and Z. Hou, *Adv. Sci.*, 2023, **10**, 2303694.
8 Z. Shan, X. Xie, X. Wu, S. Zhuang, C. Zhang and J. Orthop, *Translat.*, 2022, **36**, 184–193.
9 Y. Zhang, J. Xu, Y. C. Ruan, M. K. Yu, M. O'Laughlin, H. Wise, D. Chen, L. Tian, D. Shi, J. Wang, S. Chen, J. Q. Feng, D. H. K. Chow, X. Xie, L. Zheng, L. Huang, S. Huang, K. Leung, N. Lu, L. Zhao, H. Li, D. Zhao, X. Guo, K. Chan, F. Witte, H. C. Chan, Y. Zheng and L. Qin, *Nat. Med.*, 2016, **22**, 1160–1169.
10 T. Wu, B. Li, W. Huang, X. Zeng, Y. Shi, Z. Lin, C. Lin, W. Xu, H. Xia and T. Zhang, *Biomed. Mater.*, 2022, **17**, 35012.
11 F. Yang, Y. Xue, F. Wang, D. Guo, Y. He, X. Zhao, F. Yan, Y. Xu, D. Xia and Y. Liu, *Bioact. Mater.*, 2023, **26**, 88–101.
12 Y. Gong, P. Wang, R. Cao, J. Wu, H. Ji, M. Wang, C. Hu, P. Huang and X. Wang, *ACS Nano*, 2023, **17**, 22355–22370.
13 K. Demishtein, R. Reifen and M. Shemesh, *Nutrients*, 2019, **11**, 2363.
14 D. Predoi, C. S. Ciobanu, S. L. Iconaru, S. Raaen and K. Rokosz, *Materials*, 2023, **16**, 4412.
15 R. Vácha, F. J. Martinez-Veracoechea and D. Frenkel, *Nano Lett.*, 2011, **11**, 5391–5395.
16 J. A. Champion and S. Mitragotri, *Pharm. Res.*, 2009, **26**, 244–249.
17 N. N. M. Adnan, Y. Y. Cheng, N. M. N. Ong, T. T. Kamaruddin, E. Rozlan, T. W. Schmidt, H. T. T. Duong and C. Boyer, *Polym. Chem.*, 2016, **7**, 2888–2903.
18 B. Zhang, P. Sai Lung, S. Zhao, Z. Chu, W. Chrzanowski and Q. Li, *Sci. Rep.*, 2017, **7**, 7315.
19 Y. Fei, M. Li, Y. Li, X. Wang, C. Xue, Z. Wu, J. Xu, Z. Xiazeng, K.-Y. Cai and Z. Luo, *Nanoscale*, 2020, **12**, 16102–16112.
20 A. Kumar, A. K. Pandey, S. S. Singh, R. Shanker and A. Dhawan, *Cytometry Pt A*, 2011, **79A**, 707–712.
21 M. Guo, F. Muhammad, A. Wang, W. Qi, N. Wang, Y. Guo, Y. Wei and G. Zhu, *J. Mater. Chem. B*, 2013, **1**, 5273–5278.
22 L. A. Wallace, L. Gwynne and T. Jenkins, *Ther. Deliv.*, 2019, **10**, 719–735.
23 C. Wang, Z. Dong, Q. Zhang, M. Guo, W. Hu, S. Dong, T. Jakkree, Y. Lu and S. Du, *IET Nanobiotechnol.*, 2023, **17**, 352–359.
24 S. Han, S. Liu, Y. Song and H. Jiang, *Colloids Surf., B*, 2022, **217**, 112665.
25 N. Cao, Y. Zhao, B. Sang, Z. Wang, L. Cao, L. Sun and X. Zou, *Mater. Sci. Eng. C*, 2016, **69**, 330–336.
26 I. Tsamesidis, G. K. Pouroutzidou, E. Lymperaki, K. Kazeli, C. B. Lioutas, E. Christodoulou, P. Perio, K. Reybier, A. Pantaleo and E. Kontonasaki, *Chem. Biol. Interact.*, 2020, **318**, 108974.
27 H. Wang, D. Wang, J. Yu, Y. Zhang and Y. Zhou, *Biomater. Sci.*, 2022, **10**, 5786–5808.
28 D. Wang, J. Xing, Y. Zhang, Z. Guo, S. Deng, Z. Guan, B. He, R. Ma, X. Leng, K. Dong and Y. Dong, *Int. J. Nanomed.*, 2023, **18**, 6425–6448.
29 bing Xiao, *Master Thesis*, Shihezi University, 2017.
30 N. Hao, L. Li and F. Tang, *Biomater. Sci.*, 2016, **4**, 575–591.
31 J. Rodríguez-Sánchez, M. Á. Pacha-Olivenza and M. L. González-Martín, *Mater. Chem. Phys.*, 2019, **221**, 342–348.
32 C. A. Shahed, F. Ahmad, E. Günister, F. M. Foudzi, S. Ali, K. Malik and W. S. W. Harun, *J. Magnesium Alloys*, 2023, **11**, 3038–3058.
33 K. M. McKinnon, *Curr. Protoc. Immunol.*, 2018, **120**, 5.1.1–5.1.11.
34 A. Kamo, O. Ates Sonmezoglu and S. Sonmezoglu, *Nanoscale Adv.*, 2024, **6**, 6008–6018.
35 M. R. El-Zahry, A. Mahmoud, I. H. Refaat, H. A. Mohamed, H. Bohlmann and B. Lendl, *Talanta*, 2015, **138**, 183–189.
36 A. Reznickova, H. Y. Nguyenova, K. Zaruba, J. Strasakova, Z. Kolska, A. Michalcova, F. Prusa, O. Kvitek, P. Slepicka, P. Sajdl and V. Svorcik, *Vacuum*, 2022, **203**, 111268.
37 J. Helmlinger, C. Sengstock, C. Groß-Heitfeld, C. Mayer, T. A. Schildhauer, M. Köller and M. Epple, *RSC Adv.*, 2016, **6**, 18490–18501.